Acta Geotechnica (2024) 19:7149–7168
https://doi.org/10.1007/s11440-024-02404-x

RESEARCH PAPER

Mechanism-based shift factors to predict the fatigue performance of cemented pavement materials

Vinh T. Le[1] · **Ha H. Bui**[1] · **Giang D. Nguyen**[2] · **Jayantha Kodikara**[3] · **Didier Bodin**[4] · **James Grenfell**[4]

Received: 20 December 2023 / Accepted: 6 September 2024 / Published online: 22 September 2024

Abstract

Cemented pavement materials (CPMs) are essential components in pavement structures, yet accurately predicting their service life due to fatigue damage remains challenging. Laboratory fatigue test results are commonly employed to predict the service life of CPMs by applying a lab-to-field shift factor (SF). However, traditional approaches rely heavily on experimental data, posing challenges in ensuring the certainty of lab-to-field results. Additionally, inconsistencies in lab-to-field fatigue failure criteria further complicate SF development. To address these challenges, this study proposes a mechanism-based methodology for developing SF. This methodology comprises a rigorous two-scale fatigue model developed by the authors to characterise the fatigue performance of CPMs at the lab scale and predict their performance at the field scale, thereby facilitating the development of SFs. These SFs are established based on a consistent lab-to-field fatigue failure criterion (i.e. the modulus reduction of CPMs). By accounting for strain differences between laboratory and field scales, SFs are derived in the strain-fatigue life space. Application of this approach to typical Australian CPMs, namely siltstone and hornfels, yields mechanism-based SFs of 1.19 and 1.21, respectively.

Keywords ALF/APT tests · Cemented pavement materials · Constitutive modelling · Cohesive fatigue crack model · Lab–Field correlation · Shift factors

1 Introduction

Cemented pavement materials (CPMs), referred to as cement-stabilised pavement materials (CSPMs) or cement-treated bases (CTBs), are a mixture of granular material with cementitious binders and water. The cementitious binders may include Portland cement, blended cement, lime or other chemical binder [9]. Due to their cost-effectiveness, CPMs have gained popularity in road construction and the rehabilitation of unbound granular pavements. Therefore, the development of predictive methods of the service life is important to assist road managers in the selection and design of the CPM pavement layers. Major concerns for pavement deterioration include temperature and environmental cracking, rutting, and moisture-related issues. However, the primary mode of distress for CPMs is fatigue damage caused by repeated loading from vehicles [5]. Laboratory tests, such as unconfined compressive strength (UCS) tests, indirect tensile (IDT) tests or four-point bending (4 PB) tests, are commonly used by numerous road authorities to assess mechanical properties and the fatigue life of CPMs [10, 17, 18, 26, 27, 39]. For instance, UCS tests are commonly employed to categorise cemented material types (i.e. modified, lightly bound, and heavily bound materials) [6]. In addition, the laboratory flexural modulus of CPMs can be empirically determined from UCS [9]. However, the simplicity of the UCS test does not accurately simulate the typical behaviour of in situ CPMs, where failure frequently arises from tension. Alternatively, the IDT test is used to

---

✉ Ha H. Bui
ha.bui@monash.edu

[1] Department of Civil Engineering, Monash University, Melbourne, VIC 3800, Australia

[2] School of Architecture and Civil Engineering, The University of Adelaide, Adelaide, SA 5005, Australia

[3] ARC Industrial Transformation Research Hub (ITRH)–SPARC Hub, Department of Civil Engineering, Monash University, Melbourne, VIC 3800, Australia

[4] ARRB/NTRO Group Ltd, Port Melbourne, VIC 3207, Australia

indirectly determine the tensile properties of CPMs. The IDT test offers an effective means to replicate pavement conditions wherein tensile stresses arise from compressive loads exerted by vehicles [35, 37]. Nevertheless, a challenge encountered in the IDT fatigue test program is the signal-to-noise ratio of the linear variable differential transformers (LVDT) [2]. To overcome this problem, the 4 PB test serves as an effective method for measuring the indirect tensile strength, modulus, and fatigue life of a prismatic beam specimen [2, 8]. Additionally, the 4 PB test is regarded as a more accurate depiction of the bending stress and strain patterns experienced at the base of the CPMs in service. This is because of the analogous behaviour between the CPM layer in the field and the beam specimen subjected to the four-point bending apparatus test. Nevertheless, UCS, IDT and 4 PB tests only partially represent in situ loading and environmental conditions. This gap arises from the significant differences between laboratory and field conditions, including boundary conditions, loading conditions, stress/strain states, or material property variations. To address these disparities, translation techniques have been developed to convert laboratory fatigue life results to in-service performance predictions. These techniques often utilise a shift factor (SF) and play a crucial role in determining the fatigue life of CPMs in existing mechanistic-empirical design standards [9, 31]. However, developing a sound methodology to accurately predict SFs has been a longstanding challenge.

Due to such challenges, only a few practical standards have mentioned empirical SFs for CPMs [7, 31]. In contrast, there has been substantial research into SFs concerning conventional asphalt materials. Unlike the behaviours exhibited by CPMs, asphalt is a viscoelastic material with moduli dependent on temperature and loading rate [9, 11, 38]. However, these materials share common similarities. For example, in flexible pavements where the CPM/asphalt layer is the primary component, each is often subject to deterioration from fatigue-induced damage. Additionally, in mechanistic-empirical design standards for flexible pavements, predicting fatigue damage involves considering horizontal tensile strain at the bottom of the CPM/asphalt layer [9, 13]. Therefore, it is valuable to revisit previous studies on fatigue SFs in asphalt. It is important to note that the main target of this study is to develop SFs of CPMs in flexible pavement, while reviewing SFs in asphalt provides readers with an overview of how previous studies investigated SFs. Most previous works developed SFs by comparing laboratory fatigue tests to observed field performance, focusing on modulus reduction or fatigue cracking on the pavement surface [28]. Based on IDT fatigue tests and the performance of 15 field asphalt sections, a general SF of 10 was recommended to account for variation in the fatigue lives between laboratory and field conditions [30]. Mateos et al. [21] directly compared laboratory and field performance using two field failure criteria: 20% of the section length with any crack and 20% alligator cracking. SFs of 5.9 and 11.4 were obtained for the respective criteria. Besides, Mateos et al. [21] integrated a classical continuum fatigue model into the CalME design procedure to investigate SFs based on modulus reduction. However, this approach had limitations in accurately predicting field performance during crack growth. Al-Qadi and Nassar [1] proposed methods for determining traffic-wander and stress-state SFs, with values ranging from 1.2 to 4.5. While simple and useful for engineering applications, the lack of fatigue failure criteria information raises concerns about the reliability of these factors. Another approach presented by Ma et al. [19] estimated a laboratory-to-field SF of 0.35. This study utilised fatigue data from accelerated pavement testing (APT), or known as accelerated loading facility (ALF) testing, and 4 PB tests, incorporating an empirical fatigue damage rule. Previous findings highlight significant variations in SF values resulting from differences in the experimental methodologies used. These variations can be attributed to inconsistent fatigue failure criteria, which are modulus reduction in the laboratory compared to surface cracking in the field [21, 28], or noticeable differences in material properties observed at these scales [3]. Therefore, the development of SFs requires a robust approach that clarifies lab-to-field fatigue failure criteria and illustrates the intrinsic shifts from lab-to-field fatigue performance. Numerical methods emerge as effective tools for characterising fatigue behaviours, encompassing modulus reduction, fatigue life, and fatigue crack growth. These methods enable the development of a rational methodology for predicting SFs, offering advantages over purely experimental approaches by providing result certainty, considering intrinsic fatigue mechanisms, and accommodating diverse loading and boundary conditions. Therefore, this study proposes a mechanistic approach based on rigorous fatigue modelling for SF development, which will be presented in detail in the next section.

2 A mechanistic approach to developing mechanism-based lab-to-field SFs

In this study, the proposed mechanistic approach utilises the two-scale fatigue model developed by Le et al. [15], based on the dual-scale framework [22–25], to characterise the fatigue behaviours of CPMs and develop SFs. As presented in Le et al. [15], this fatigue model successfully captured fatigue responses in cemented materials, including reproducing three distinct stages of the fatigue curve, describing hysteresis behaviour, and effectively accounting for the significant impact of stress level amplitudes on material fatigue lives, while maintaining mesh independence results. Therefore, this fatigue model provides a reliable framework for developing SFs. The proposed methodology for SF development in this paper is presented in Fig. 1 as a flowchart. Initially, the two-scale fatigue modelling approach is validated using experimental laboratory data from 4 PB tests. Subsequently, this validated model is employed to predict the field performance of ALF tests. Based on the numerical results obtained, SFs are found, accounting for the variations in strain between the laboratory and field scales. This proposed methodology distinguishes itself from previous studies that solely relied on experiments since it employs a rigorous fatigue modelling approach for characterising the fatigue performance of CPMs when shifting from laboratory to field scales, ultimately leading to the development of SFs. Therefore, the proposed approach helps reduce uncertainty in material properties at both scales. Furthermore, the developed SFs are based on a consistent lab-to-field fatigue failure criterion, which is the reduction in modulus of CPMs.

The proposed methodology for SF development is structured as follows: Sect. 2.1 provides a brief overview of the two-scale framework and the cohesive fatigue model. In Sect. 2.2, the validation of the two-scale fatigue model and the examination of fatigue failure in CPMs under 4 PB tests are presented. This is followed by the prediction of CPMs' field performance and the discussion of associated fatigue failures in Sect. 2.3. The method used for developing SFs is detailed in Sect. 2.4.

2.1 Two-scale modelling for fatigue cracking

The primary contribution of this paper lies in the application of the two-scale fatigue model [15] to the development of SFs. Therefore, this section only summarises the two-scale continuum constitutive framework, which incorporates two fracture planes (two cracks). The fundamental concepts and essential formulations of this framework are explained, along with the novel cohesive-frictional fatigue model employed to represent the fatigue responses of the fracture planes.

2.1.1 Two-scale framework

An RVE denoted as Ω is defined, which consists of two fracture planes Ω_k ($k = 1{,}2$) and an outer bulk material Ω_o, as depicted in Fig. 2. The fracture planes possess a thickness l_k and an area A_k represented by the normal vector $\mathbf{n}_k$. The nominal size of the RVE is defined as $L_k = \Omega_k / A_k$. By employing mixture theory, the volume-averaged total strain rate can be decomposed into the outer and inner strain rates of the fracture planes.

$$\dot{\boldsymbol{\varepsilon}} = f_1 \dot{\boldsymbol{\varepsilon}}_{i1} + f_2 \dot{\boldsymbol{\varepsilon}}_{i2} + (1 - f_1 - f_2)\dot{\boldsymbol{\varepsilon}}_{\mathrm{o}} \tag{1}$$

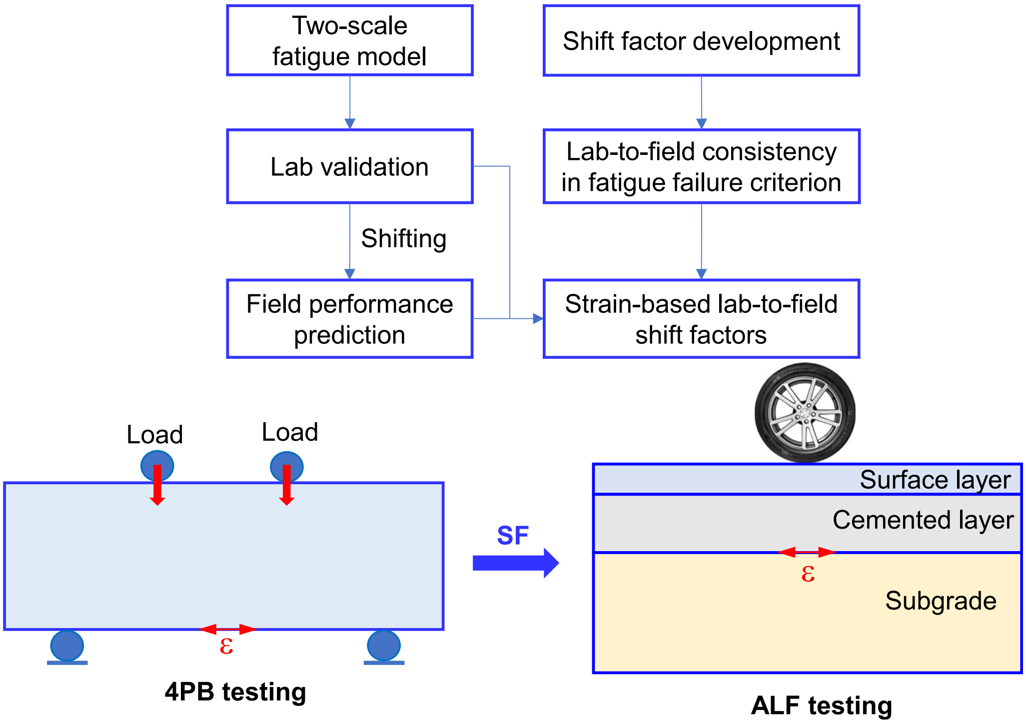

Fig. 1 Proposed methodology for SF development

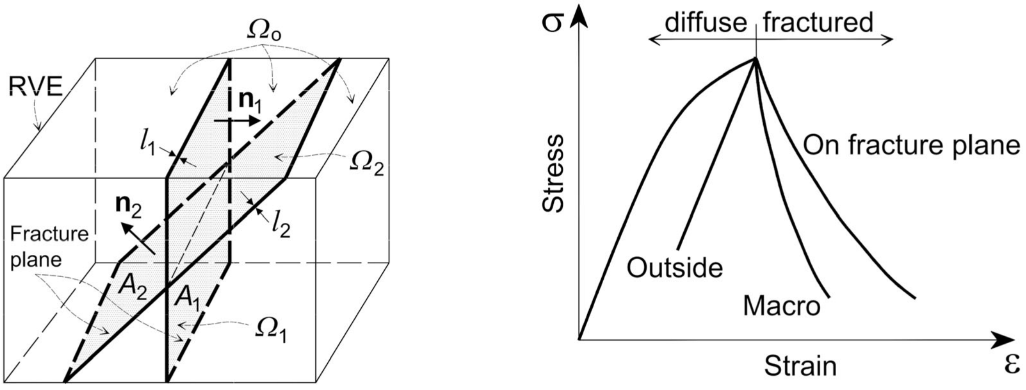

(a) (b)

Fig. 2 **a** Illustration of an RVE embedded 2 fracture planes; **b** Material responses can be categorised into two stages: pre-fracture (diffuse) and post-fracture (after [15])

where $\dot{\boldsymbol{\varepsilon}}_o$ and $\dot{\boldsymbol{\varepsilon}}_{ik}$ represent the strain rate tensors outside and inside the fracture planes, respectively, and f_k denotes the volume fraction of the fracture planes, which is given by $f_k = l_k/L_k$.

Considering extremely thin fracture planes in quasi-brittle materials ($l_k \ll L_k$), the strain rate tensor inside the fracture plane can be approximated [33, 36]:

$$\dot{\boldsymbol{\varepsilon}}_{i1} = \frac{1}{l_1}\mathbf{n}_1\dot{\mathbf{u}}_1 \text{and} \dot{\boldsymbol{\varepsilon}}_{i2} = \frac{1}{l_2}\mathbf{n}_2\dot{\mathbf{u}}_2 \tag{2}$$

where $\dot{\boldsymbol{u}}_k$ represents the displacement jump rate across the fracture planes.

To establish a connection between the response inside and outside the fracture planes and the overall behaviour of the RVE, the virtual work equation [12] is employed:

$$\boldsymbol{\sigma}^T\dot{\boldsymbol{\varepsilon}} = f_1\boldsymbol{\sigma}_{i1}^T\dot{\boldsymbol{\varepsilon}}_{i1} + f_2\boldsymbol{\sigma}_{i2}^T\dot{\boldsymbol{\varepsilon}}_{i2} + (1 - f_1 - f_2)\boldsymbol{\sigma}_o^T\dot{\boldsymbol{\varepsilon}}_o \tag{3}$$

where $\boldsymbol{\sigma}_o$ and $\boldsymbol{\sigma}_{ik}$ are the stress tensors outside and inside the fracture planes, respectively.

By using Eqs. (1), (2), and considering the conditions $f_1 \to 0$,$f_2 \to 0$ resulting from the presence of very thin fracture planes, Eq. (3) can be reformulated as follows:

$$\begin{aligned}&\left(\boldsymbol{\sigma}^T - \boldsymbol{\sigma}_o^T\right)\dot{\boldsymbol{\varepsilon}}_o + \frac{1}{L_1}\left(\boldsymbol{\sigma}^T\mathbf{n}_1 - \boldsymbol{\sigma}_{i1}^T\mathbf{n}_1\right)\dot{\mathbf{u}}_1\\ &\quad + \frac{1}{L_2}\left(\boldsymbol{\sigma}^T\mathbf{n}_2 - \boldsymbol{\sigma}_{i2}^T\mathbf{n}_2\right)\dot{\mathbf{u}}_2\\ &\quad = 0\end{aligned} \tag{4}$$

Further simplification of Eq. (4) can be achieved by employing the definition of traction on the fracture planes, $\mathbf{t}_1^{\mathrm{T}} = \boldsymbol{\sigma}_{i1}^{\mathrm{T}}\mathbf{n}_1$ and $\mathbf{t}_2^{\mathrm{T}} = \boldsymbol{\sigma}_{i2}^{\mathrm{T}}\mathbf{n}_2$, resulting in the following expression:

$$\left(\boldsymbol{\sigma}^T - \boldsymbol{\sigma}_o^T\right)\dot{\boldsymbol{\varepsilon}}_o + \frac{1}{L_1}\left(\boldsymbol{\sigma}^T\mathbf{n}_1 - \mathbf{t}_1^T\right)\dot{\mathbf{u}}_1 + \frac{1}{L_2}\left(\boldsymbol{\sigma}^T\mathbf{n}_2 - \mathbf{t}_2^T\right)\dot{\mathbf{u}}_2 = 0 \tag{5}$$

To fulfil Eq. (5) for any arbitrary values of $\dot{\boldsymbol{\varepsilon}}_o$,$\dot{\mathbf{u}}_1$ and $\dot{\mathbf{u}}_2$, the following conditions must be satisfied: $\boldsymbol{\sigma} = \boldsymbol{\sigma}_{\mathrm{o}} = \mathbf{a}_{\mathrm{o}}\boldsymbol{\varepsilon}_{\mathrm{o}}$, $\mathbf{n}_1^{\mathrm{T}}\boldsymbol{\sigma} = \mathbf{t}_1$, $\mathbf{n}_2^{\mathrm{T}}\boldsymbol{\sigma} = \mathbf{t}_2$. The relationship between the rates of traction and displacement jump can be expressed as follows:$\dot{\mathbf{t}}_1 = \mathbf{K}_1^{\mathrm{t}}\dot{\mathbf{u}}_1$ and $\dot{\mathbf{t}}_2 = \mathbf{K}_2^{\mathrm{t}}\dot{\mathbf{u}}_2$, where $\mathbf{K}_1^{\mathrm{t}}$, $\mathbf{K}_2^{\mathrm{t}}$ denote the tangent stiffness matrix of fracture planes 1 and 2 in the global coordinate system, respectively.

Substituting Eq. (1), the rate forms $\dot{\mathbf{t}}_1 = \mathbf{K}_1^{\mathrm{t}}\dot{\mathbf{u}}_1$, $\dot{\mathbf{t}}_2 = \mathbf{K}_2^{\mathrm{t}}\dot{\mathbf{u}}_2$, $\dot{\boldsymbol{\sigma}}_{\mathrm{o}} = \mathbf{a}_{\mathrm{o}}\dot{\boldsymbol{\varepsilon}}_{\mathrm{o}}$ into the rate form of traction continuity ($\mathbf{n}_1^{\mathrm{T}}\dot{\boldsymbol{\sigma}} = \dot{\mathbf{t}}_1$, $\mathbf{n}_2^{\mathrm{T}}\dot{\boldsymbol{\sigma}} = \dot{\mathbf{t}}_2$), the velocity jumps of the two cracks can be computed as follows:

$$\begin{bmatrix}\dot{\mathbf{u}}_1\\ \dot{\mathbf{u}}_2\end{bmatrix} = \begin{bmatrix}\mathbf{M}_1 & \mathbf{M}_2\\ \mathbf{M}_3 & \mathbf{M}_4\end{bmatrix}^{-1}\begin{bmatrix}\mathbf{n}_1^{\mathrm{T}}\mathbf{a}_{\mathrm{o}}\\ \mathbf{n}_2^{\mathrm{T}}\mathbf{a}_{\mathrm{o}}\end{bmatrix}\dot{\boldsymbol{\varepsilon}} = \begin{bmatrix}\mathbf{V}_1\\ \mathbf{V}_2\end{bmatrix}\dot{\boldsymbol{\varepsilon}} \tag{6}$$

where $\mathbf{V}_{i(i=1,2)}$ is 4-by-4 matrix for 2D case and 6-by-6 matrix for 3D case, respectively, and $\mathbf{M}_{i(i=1,4)}$ is defined as follows:

$$\begin{aligned}\mathbf{M}_1 &= \frac{1}{L_1}\mathbf{n}_1^{\mathrm{T}}\mathbf{a}_{\mathrm{o}}\mathbf{n}_1 + \mathbf{K}_1^{\mathrm{t}};\ \mathbf{M}_2 = \frac{1}{L_2}\mathbf{n}_1^{\mathrm{T}}\mathbf{a}_{\mathrm{o}}\mathbf{n}_2\\ \mathbf{M}_3 &= \frac{1}{L_1}\mathbf{n}_2^{\mathrm{T}}\mathbf{a}_{\mathrm{o}}\mathbf{n}_1;\ \mathbf{M}_4 = \frac{1}{L_2}\mathbf{n}_2^{\mathrm{T}}\mathbf{a}_{\mathrm{o}}\mathbf{n}_2 + \mathbf{K}_2^{\mathrm{t}}\end{aligned} \tag{7}$$

By employing the rate form $\dot{\boldsymbol{\sigma}}_{\mathrm{o}} = \mathbf{a}_{\mathrm{o}}\dot{\boldsymbol{\varepsilon}}_{\mathrm{o}}$, along with Eqs. (1), (6), and considering the conditions $f_1 \to 0$ and $f_2 \to 0$, the macro-stress–strain relationship can be derived as follows:

$$\dot{\boldsymbol{\sigma}} = \left[\mathbf{a}_{\mathrm{o}} - \frac{1}{L_1}\mathbf{a}_{\mathrm{o}}\mathbf{n}_1\mathbf{V}_1 - \frac{1}{L_2}\mathbf{a}_{\mathrm{o}}\mathbf{n}_2\mathbf{V}_2\right]\dot{\boldsymbol{\varepsilon}} \tag{8}$$

2.1.2 Cohesive crack model

This section summarises the developed cohesive-frictional fatigue model to describe the behaviour of the fracture planes [15]. The displacement jumps, $\mathbf{u}_c$, occurring between the two fracture surfaces, can be separated into elastic ($\mathbf{u}^e$), plastic ($\mathbf{u}_c^p$), and fatigue ($\mathbf{u}_c^f$) constituents in the following manner:

$$\mathbf{u}_c = \mathbf{u}_c^e + \mathbf{u}_c^p + \mathbf{u}_c^f \tag{9}$$

The traction–displacement relationship takes the following form:

$$\mathbf{t}_c = \begin{bmatrix} t_n \\ t_{s1} \\ t_{s2} \end{bmatrix} = \begin{bmatrix} K_n[1 - DH(t_n)] & 0 & 0 \\ 0 & K_s(1-D) & 0 \\ 0 & 0 & K_s(1-D) \end{bmatrix} \begin{bmatrix} u_n - u_n^p - u_n^f \\ u_{s1} - u_{s1}^p - u_{s1}^f \\ u_{s2} - u_{s2}^p - u_{s2}^f \end{bmatrix} = \mathbf{K}_c^s(\mathbf{u}_c - \mathbf{u}_c^p - \mathbf{u}_c^f) \tag{10}$$

where $\mathbf{K}_c^s$, which represents the secant stiffness matrix of the cohesive fracture plane; K_n and K_s, denoting the elastic stiffness in the normal and shear directions, respectively; t_n,t_{s1}, and t_{s2}, representing the normal and shear tractions acting on the two surfaces of the fracture planes; D, the damage variable; u_n, u_{s1}, and u_{s2}, indicating the total normal and shear displacements; u_n^p, u_{s1}^p,u_{s2}^p,u_n^f, u_{s1}^f, and u_{s2}^f, denoting the plastic and fatigue normal and shear displacements, respectively; and $H(t_n)$ is the Heaviside step function.

2.1.2.1 Bounding/yielding surface

The equation of the bounding surface is as follows:

$$y(t_n, t_s, D) = \left(\frac{t_n - A}{B}\right)^2 - \left(\frac{t_s}{C}\right)^2 - 1 = 0 \tag{11}$$

where $t_s^2 = t_{s1}^2 + t_{s2}^2$, $A = (1-D)f_t^0 + B$, $B = C^0(1-D)/[2(1-D) + 2D\mu^2]$, and $C = B\sqrt{(1-D) + D\mu^2}$, in which $\mu = \tan(\varphi)$ represents the material internal friction coefficient with φ being the friction angle; f_t^0, the tensile strength of the material; and C^0, initial cohesion.

The total damage variable D in Eq. (11) is expressed as the sum static damage increment ($\dot{D}_s$) induced by static loads and fatigue damage increment ($\dot{D}_f$) caused by cyclic loadings:

$$D = \sum\left(\dot{D}_s + \dot{D}_f\right) \tag{12}$$

The non-associated plastic potential is used in this study to describe the dilation and plastic deformation on the fracture planes, and its formulation is written as:

$$g(t_n, t_s, D) = \left(\frac{t_n - A}{B}\right)^2 - \gamma\left(\frac{t_s}{C}\right)^2 - 1 = 0 \tag{13}$$

where γ being the parameter that controls the non-associativity, hence, the non-associated flow rules are defined as:

$$\dot{u}_n^p = \frac{-\frac{\partial y}{\partial \mathbf{t}_c}\frac{\partial \mathbf{t}_c}{\partial \mathbf{u}_c}\dot{\mathbf{u}}_c}{S_B}\frac{\partial g}{\partial t_n}; \dot{u}_s^p = \frac{-\frac{\partial y}{\partial \mathbf{t}_c}\frac{\partial \mathbf{t}_c}{\partial \mathbf{u}_c}\dot{\mathbf{u}}_c}{S_B}\frac{\partial g}{\partial t_s} \tag{14}$$

where S_B represents the plastic softening modulus associated with the bounding surface.

The interaction between static damage and fatigue damage is considered in the following manner:

$$\dot{D}_s = e^{-u_{ps}}\dot{u}_{ps}\left(1 - D_f\right) \text{ with} \dot{u}_{ps} = \frac{1}{\delta_s}\sqrt{\left(\alpha\dot{u}_n^p\right)^2 + \beta\left[\left(\dot{u}_{s1}^p\right)^2 + \left(\dot{u}_{s2}^p\right)^2\right]} \tag{15}$$

where $u_{ps} = \sum\dot{u}_{ps}$ denotes the accumulated plastic displacement parameter; the non-dimensional parameters α and β represent the contributions of normal and shear plastic displacements, respectively, to the damage evolution; the relative displacement, δ_s, is used for normalising $\dot{u}_{ps}$ and is set to 0.01 mm for all simulations conducted in this study.

2.1.2.2 Subloading/fatigue surface

The equation for the subloading surface is represented by a standard hyperbola:

$$y_o(t_n, t_s, X_n) = \left[\left(\frac{t_n - a - X_n}{b}\right)^2 - \left(\frac{t_s}{c}\right)^2 - 1\right]\eta = 0 \tag{16}$$

where $a = (1-\psi)f_t^0 + b$, $b = C^0(1-\psi)/[2(1-\psi) + 2\psi\mu^2]$, and $c = b\sqrt{(1-\psi) + \psi\mu^2}$; ψ, the parameter that determines the initial position of subloading surface in the stress space and evolves as damage develops; X_n, the kinematic hardening parameter that controls the current position of subloading surface; and η, the parameter with $\eta = 1$ for the top subloading surface and $\eta = -1$ for the bottom subloading surface (Fig. 3a).

In the stress space, the subloading surface is a region bounded by the top and bottom subloading surfaces, defined as follows:

$$\psi_t = \psi_b - e_{do}(0 \le \psi_t \le 1; 0 \le \psi_b \le 1; 0 \le e_{do} \le 1) \tag{17}$$

The elastic domain in Eq. (17) decides the size of the subloading surface and is defined as:

$$e_{do} = e_{do}^0(1 - D) \tag{18}$$

where parameter e_{do}^0 represents the initial value of the elastic domain.

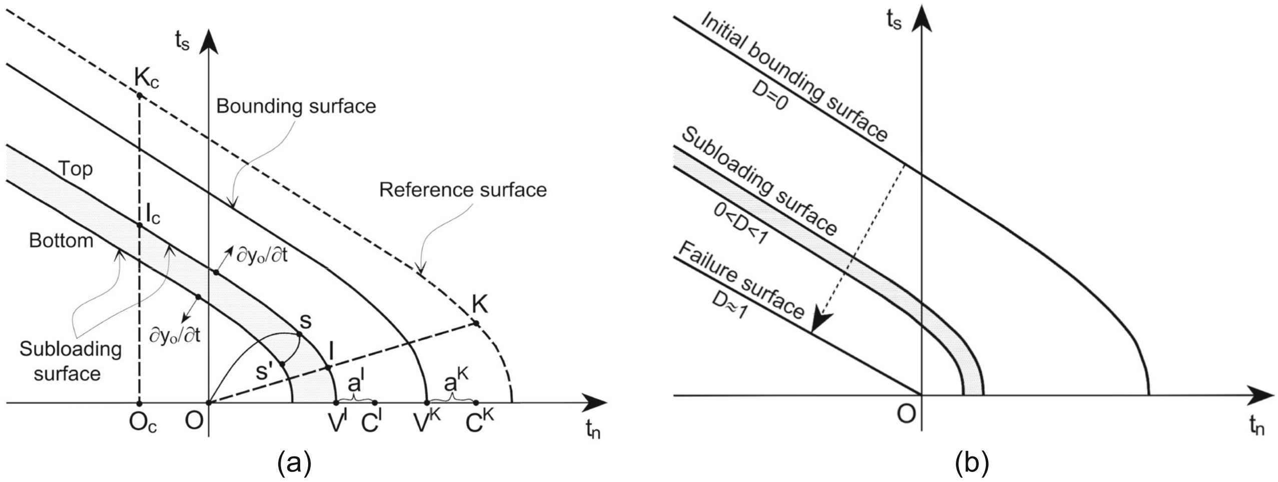

Fig. 3 **a** The vertices and centres of bounding and subloading surfaces in the stress space; **b** The shrinkage of the bounding surface and subloading surface upon damage evolution (after [15])

The non-associated fatigue flow rule can be expressed as follows:

$$\dot{u}_n^f = \frac{-\frac{\partial y_0}{\partial \mathbf{t}_c}\frac{\partial \mathbf{t}_c}{\partial \mathbf{u}_c}\dot{\mathbf{u}}_{\boldsymbol{c}}}{S_I}\frac{\partial g_0}{\partial t_n}; \dot{u}_s^f = \frac{-\frac{\partial y_0}{\partial \mathbf{t}_c}\frac{\partial \mathbf{t}_c}{\partial \mathbf{u}_c}\dot{\mathbf{u}}_{\boldsymbol{c}}}{S_I}\frac{\partial g_0}{\partial t_s} \tag{19}$$

where g_0 is the fatigue potential function of the subloading surface, and is described as:

$$g_o(t_n, t_s, X_n) = \left[\left(\frac{t_n - a - X_n}{b}\right)^2 - \gamma\left(\frac{t_s}{c}\right)^2 - 1\right]\eta = 0 \tag{20}$$

The fatigue-induced damage mechanism in both tension-shear and compression-shear domains is considered with the value of S_I in Eq. (19) determined using the interpolation rule:

$$S_I = \begin{cases} \dfrac{S_K}{e^{-\frac{IK}{OK}Q}\left(1 - \dfrac{IK}{OK}\right)^{\kappa}}, t_n \geq 0 \\ \dfrac{S_K}{e^{-\frac{IK}{OK}Q}\left(1 - \dfrac{I_cK_c}{O_cK_c}\right)^{\kappa}}, t_n < 0 \end{cases} \tag{21}$$

where Q and κ are parameters that govern the magnitude of the fatigue flow rule; S_K represents the softening modulus of the image point evaluated on the reference surface (as shown in Fig. 3a).

To characterise the progression of fatigue-induced damage under fatigue loads, the incremental fatigue damage variable is defined as:

$$\dot{D}_f = h(D)\dot{u}_{pf}\text{with}\dot{u}_{pf} = \frac{1}{\delta_f}\sqrt{\left(\alpha\dot{u}_n^f\right)^2 + \beta\left[\left(\dot{u}_{s1}^f\right)^2 + \left(\dot{u}_{s2}^f\right)^2\right]} \tag{22}$$

where the relative displacement δ_f is used to normalise $\dot{u}_{pf}$; the competition factor $h(D)$ accounts for the competitive mechanism during the three distinct processes of fatigue damage evolution [16, 29], and is defined as follows:

$$h(D) = \min\left(e^{-m_1 D} + e^{-m_2(1-D)}, 1\right) \tag{23}$$

where m_1 and m_2 are fatigue parameters; and the terms $e^{-m_1 D}$ and $e^{-m_2(1-D)}$ signify the reduction and increase, respectively, of the fatigue damage rate throughout the cyclic loading process.

Besides the fatigue flow and fatigue damage rules, the kinematics of the subloading surface and cycle jump technique play a vital role in the fatigue crack model. A detailed description of these rules can be referred to Le et al. [15]. By incorporating the cohesive-frictional fatigue crack model, the two-scale framework presented in Sect. 2.1.1 can be utilised and implemented in any numerical method for simulating boundary value applications.

2.2 Validation of CPMs' fatigue characteristics at laboratory testing

This section is focused on characterising the CPMs' fatigue behaviour characterisation in the laboratory using the fatigue model [15] presented in Sect. 2.1. The model is implemented into ABAQUS for structural analysis, utilising the VUMAT subroutine. For this purpose, 4 PB tests of two cemented materials, namely siltstone and hornfels [2], are simulated. The tests include strength tests and fatigue

Table 1 Material properties of siltstone and hornfels materials used in experimental laboratory and ALF tests (after [2])

Materials	Cement content (%)	Maximum dry density (t/m^3)	Optimum moisture content (%)	Plasticity index	Plastic limit	Liquid limit
Siltstone	4	2.070	8.0	6	15	21
Hornfels	3	2.325	6.1	5	–	22

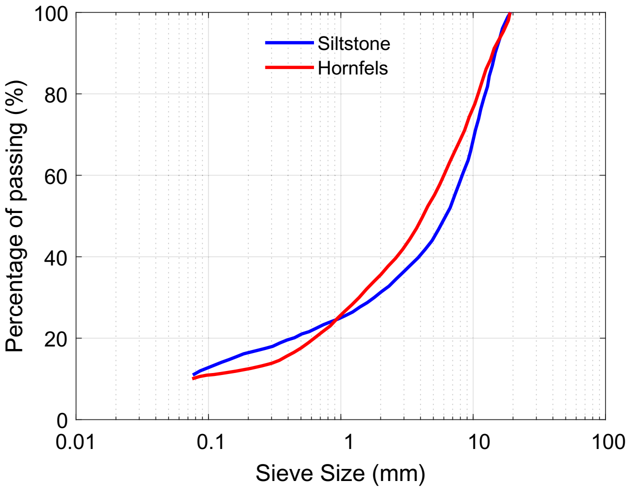

Fig. 4 Particle size distribution for the siltstone and hornfels materials (after [2])

tests. The experimental material properties of siltstone and hornfels materials are summarised in Table 1, while Fig. 4 presents particle size distribution for both materials. It is important to note that the CPMs used in the 4 PB tests are identical to the ones used in ALF tests in Sect. 2.3, as reported in Austroads [2].

Table 2 summarises the mechanical parameters of the materials and model parameters required for the fatigue cohesive-frictional models. It is important to note that strength tests are carried out initially to determine the mechanical properties of the materials and elastoplastic parameters. Based on these results, the fatigue parameters are calibrated from the fatigue experiments. Furthermore, the strength test provides the maximum load that the specimen can withstand. This maximum load is then used to estimate the maximum cyclic applied load in the fatigue test.

2.2.1 Simulation set-up

Figure 5a illustrates the 4 PB beam testing geometry and boundary conditions. To reduce the simulation time, the symmetry half of the beam is utilised with two different mesh configurations, mesh 1 (1570 elements) and mesh 2 (2383 elements), as depicted in Fig. 5b, c. The strength test is performed under force-controlled mode. During the loading process, the applied load (P) and the deflection at the midpoint (δ) are recorded. Based on the recorded data, the flexural stress, flexural strain, and flexural modulus can be calculated using the elastic beam theory [8]:

$$\varepsilon_f = \frac{108H\delta}{23L^2} \tag{24}$$

$$\sigma_f = \frac{PL}{BH^2} \tag{25}$$

$$E_f = \frac{23P_mL^3}{108\delta_mBH^3} \tag{26}$$

where ε_f represents flexural strain, L stands for span length, H is mean beam height, B is mean beam width, σ_f is flexural stress, E_f is the flexural modulus, P_m represents

Table 2 Mechanical properties and calibrated model parameters for two different CPMs

Properties	Siltstone	Hornfels
E_c(GPa)	9	18
v	0.2	0.2
C^0(MPa)	7.5	7.5
f_t^0(MPa)	0.6	0.7
Elasto-plastic parameters		
K_n=K_s (Pa/m)	5.2×10^{13}	7.0×10^{13}
μ	0.364	0.364
α	0.5	0.5
β	0.01	0.01
γ	1.5	1.5
Fatigue parameters		
ψ_t^{ini}	0.4	0.4
e_{do}^0	0.05	0.05
Q	11	13
δ_f(m)	2.5×10^{-7}	1×10^{-7}
κ	3	2.5
m_1	20	20
m_2	5	5
G_c(N/m)	30	40
C_{jump}	0.3	0.2
m_{jump}	1.0	1.0

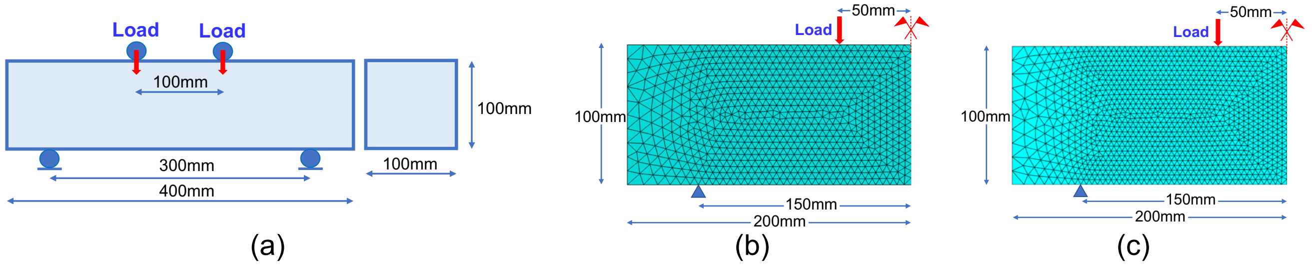

Fig. 5 Specimen geometry and mesh sizes for the 4 PB test: **a** Geometry; **b** Mesh 1 in ABAQUS; **c** Mesh 2 in ABAQUS

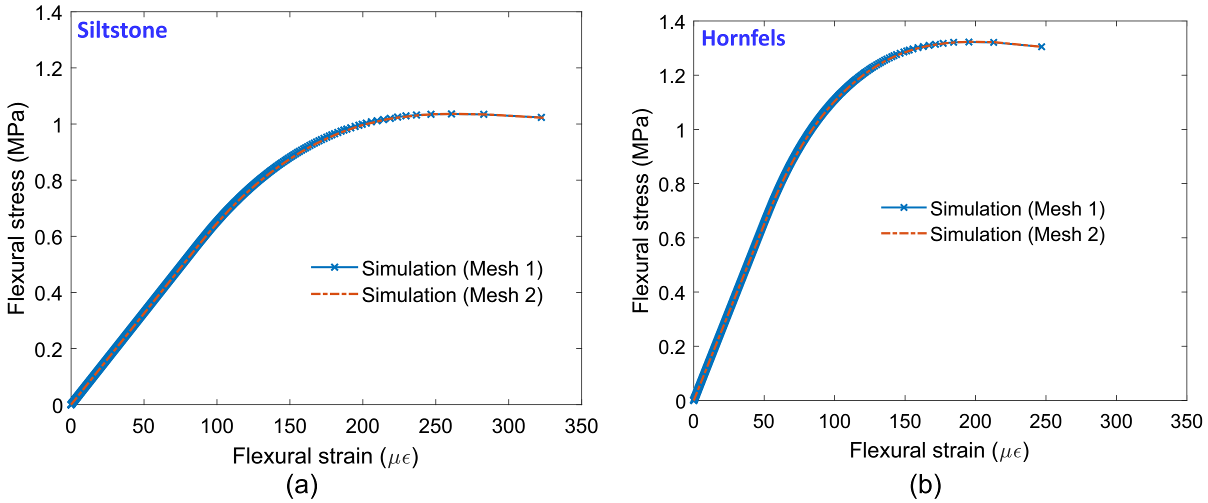

Fig. 6 Stress–strain responses for strength tests of 4 PB beams: **a** Siltstone materials; **b** Hornfels materials

maximum cyclic load magnitude, and δ_m corresponds to the deflection at P_m.

2.2.2 Strength test validation

The simulation results of the 4 PB strength tests are presented in Fig. 6. The stress–strain curves illustrate elastic behaviour in the initial stage, followed by hardening behaviour until the sample suddenly ruptures. The numerical convergence upon mesh refinement is demonstrated by consistent outcomes with two different meshes in Fig. 6. This convergence is thanks to the introduction of the characteristic length in the two-scale framework. As experimental data on stress–strain curves are limited, a comparison of flexural strength (FS) between experimental data and simulation results is shown in Table 3, revealing slightly different results compared but confirming the validity of calibrated parameters against the experiment.

Table 3 Comparison of flexural strength between simulation results and experimental data

Cemented materials	Flexural strength (FS) (MPa)		Difference (%)
	Simulation	Experiment	
Siltstones	1.04	1.06	2
Hornfels	1.32	1.26	5

2.2.3 Fatigue tests at the laboratory scale

2.2.3.1 Fatigue performance under one specific stress level The primary objective of this section is to illustrate the fatigue failure of 4 PB beams constructed from CPMs. This illustration will be compared with the fatigue failure of CPMs observed in the full-scale testing under ALF loading, as discussed in Sect. 2.3.2. Using the results obtained from the strength test described in Sect. 2.2.2, the fatigue test in this section is conducted through a stress-controlled program with a load frequency of 40 Hz. The maximum loads applied during the fatigue tests are determined as a percentage of the peak load from the strength tests, while the minimum load is set at 50 N.

Figure 7 shows the predictive modulus reduction curve for the 4 PB fatigue test conducted on siltstone materials at a stress level of 70%FS. The curve displays three distinct phases: an initial drop in the first phase, followed by a steady decrease in the second phase, and finally, a rapid

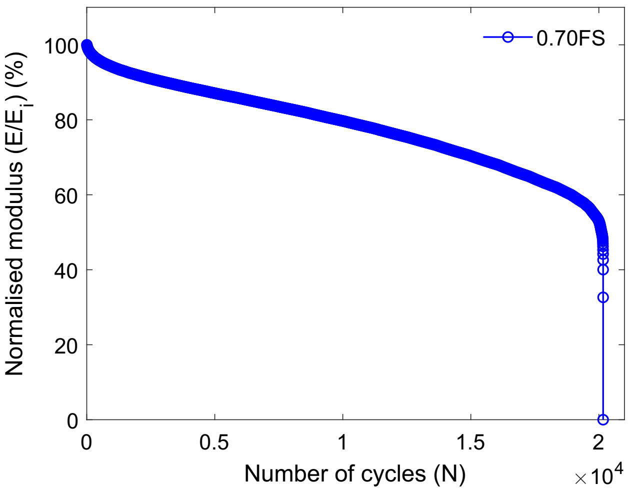

Fig. 7 Predictive modulus reduction curve of the 4 PB fatigue test at the stress level of 70%FS for siltstone materials

decline in the final phase. These three distinct phases are commonly observed in the fatigue tests of CPMs [14, 20, 32].

Figure 8 presents the details of a 4 PB beam fatigue test conducted on siltstone materials at a stress level of 70%FS, with varying numbers of cycles. The macro-behaviour of the specimen is depicted by the residual horizontal tensile stress zone, which initially forms at the bottom and middle of the beam (Fig. 8a). As the number of cycles increases, this zone expands upward, accompanied by a decrease in the horizontal stress values. This expansion and reduction indicate the occurrence of softening behaviour in the specimen. Likewise, the zone of normal traction on the primary cracks initially appears at the bottom of the beam. With cyclic loading, this zone also expands upward, signifying a decrease in material strength as indicated by reduced normal traction values.

The softening behaviour observed in the horizontal stress and normal traction is closely related to the development of the damage variable, as shown in Fig. 8c. The damage zone grows with repeated loading. In the first cycle, this zone initiates at the middle bottom of the specimen, reaching a maximum damage value of 0.012. However, at cycle 9176, the damage zone tends to spread in the middle region of the specimen. In the last cycles, the specimen ultimately fails suddenly with a bottom-up damaged domain and a maximum damage value of 0.509 (Fig. 6c).

Regarding the initiation and evolution of the fatigue crack zone (FCZ), Fig. 9 illustrates its development at different stages of the fatigue test. In the first cycle, the FCZ emerges extensively at the bottom and middle of the specimen. Mode-I failure occurs at the centre and bottom of the beam, with cracks propagating in the vertical direction. With additional cyclic loading, the FCZ increases in size and shifts upward, characterised by new crack initiation and propagation. The evolution of the FCZ is

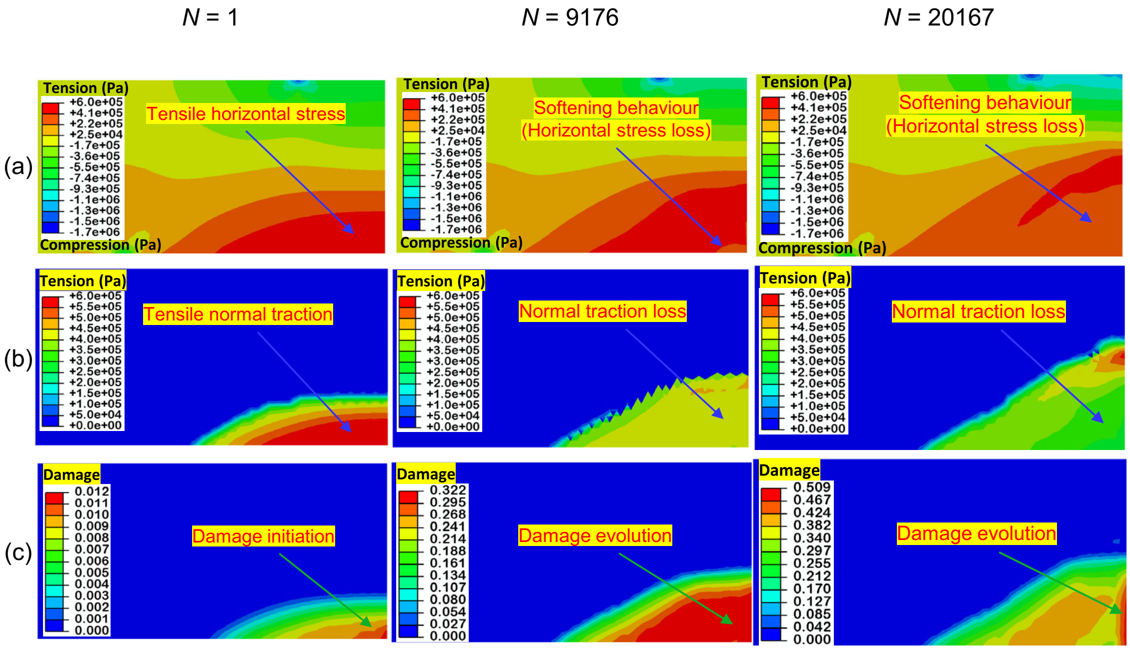

Fig. 8 Details of 4 PB beam fatigue test at a stress level of 70%FS for siltstone materials under the different number of cycles: **a** Horizontal stress evolution (Pa); **b** Evolution of normal traction on primary crack (Pa); **c** Evolution of maximum total damage contour profiles

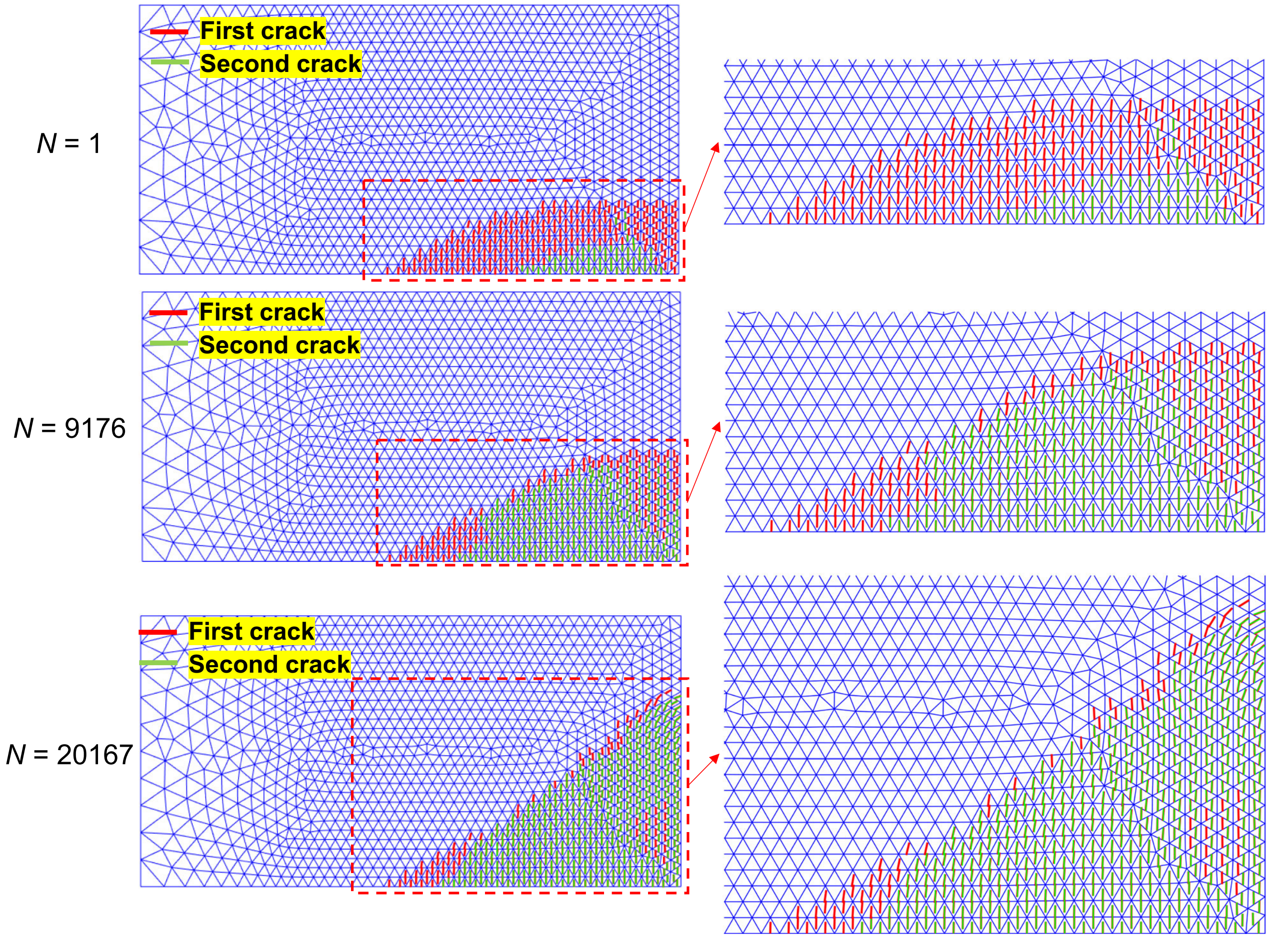

Fig. 9 Fatigue crack evolution of 4 PB beam fatigue test at a stress level of 70%FS for siltstone materials under the different number of cycles

attributed to the loss of material strength in the specimen, which aligns with the findings in Fig. 8c.

2.2.3.2 Fatigue performance under different stress levels

We conducted the fatigue tests on two materials under various stress levels, ranging from 60 to 95% of their respective FSs determined in the strength tests. Figure 10a and b displays the modulus reduction curves with absolute cycles for siltstone and hornfels materials, respectively. The beams experience early failure as the stress levels increase. To qualitatively demonstrate the impact of stress levels on modulus reduction, normalised cycle curves are plotted in Fig. 10c and d. These curves indicate that the value of modulus reduction at failure (i.e. when the normalised cycle value is equal to 1) is higher for larger stress levels, resulting in an upward shift in the normalised modulus reduction curves. This phenomenon occurs because, at increased stress levels, the damage tends to concentrate on damaged areas, leading to specimen failure without sufficient cumulative growth of fatigue damage. This damage is the main cause of the reduction in modulus. As a result, beams subjected to higher stress levels experience a smaller decrease in modulus at the failure stage.

To assess the reliability of the proposed model in capturing the fatigue response of the material under different stress levels, a comparison of fatigue performances between simulations and experiments is presented in Fig. 11. The comparison is based on the relationship between the initial micro-tensile strain measuring at the middle bottom point of the beam and fatigue lives (S-N_f curves). It is noted that N_f is defined as the cycle to reach a 50% decrease in modulus, according to Austroads [8]. The proposed model effectively captures the significant influence of load level amplitudes on fatigue lives, as evidenced by the satisfactory agreement between the simulation trend line and the experimental data.

2.3 Prediction of CPMs' fatigue characteristic at field testing

Based on the calibrated parameters presented in Sect. 2.2, the fatigue performance of CPMs at the field scales is

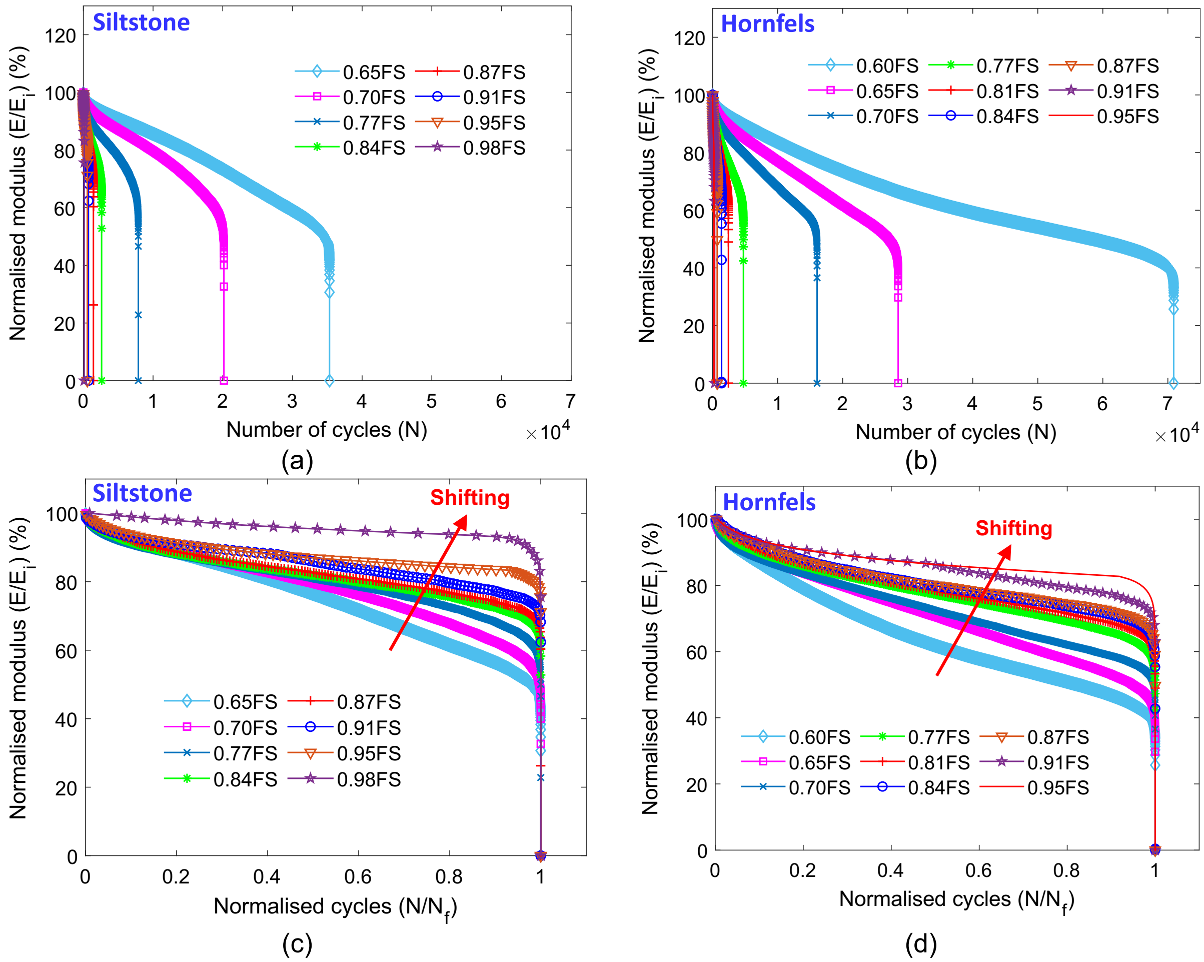

Fig. 10 Predictive modulus reduction curves of 4 PB beams at different stress levels: **a** Absolute cycle curves for siltstone materials; **b** Absolute cycle curves for hornfels materials; **c** Normalised cycle curves for siltstone materials; **d** Normalised cycles for hornfels materials

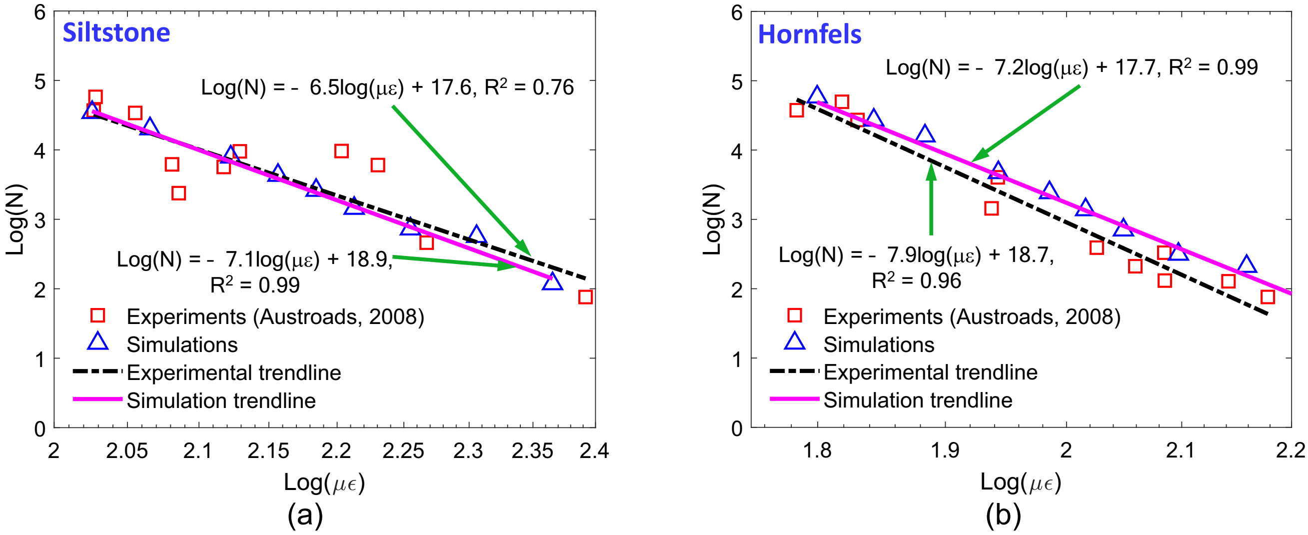

Fig. 11 Comparison of initial micro-tensile tensile strain versus fatigue lives (S-N_f curves) between simulation and experiments: **a** Siltstone materials; **b** Hornfels materials

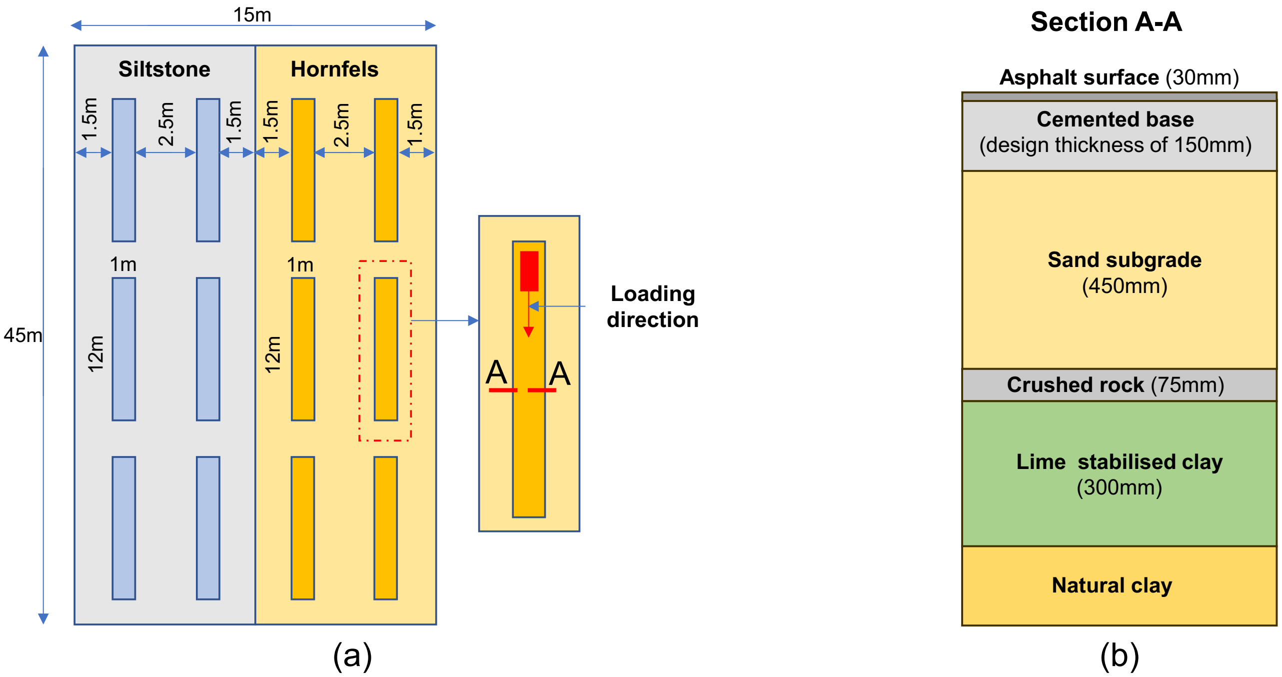

Fig. 12 ALF tests: **a** Experiment layout; **b** Test pavement structure

predicted in this section. To achieve this, simulations of the full-scale testing under ALF loading [3] are conducted. As mentioned in Sect. 2.2, the CPMs used in the ALF tests are identical to the ones used in the 4 PB tests.

2.3.1 Experiment layout plan and simulation set-up

The experiment layout plan for the ALF tests conducted by the Australian Road Research Board (ARRB) [3, 4] is presented in Fig. 12a. The study involved the construction of two test pavement sections made of two different CPMs: siltstone and hornfels. Each experimental layout consisted of 7.5 m wide by 45 m long cemented pavement sections, with the potential for up to six ALF experiments for each CPM. Before applying the ALF loads, the hornfels and siltstone CPM layers were cured for 4 and 7 months, respectively. The test pavement sections were continuously loaded with rolling half-axle wheel loads, with a dual wheel load. The load capacities ranged from 40 to 80 kN. It is worth noting that all experiments were conducted under dry conditions as testing was undertaken indoors. Therefore, the moisture conditions of the CPM and subgrade layers were controlled, as detailed in Appendix G of Austroads [4]. During the ALF testing, a rolling wheel travelled on the 12 m sections of pavement in one direction. The initial design of the ALF test sections included 150 mm-thick CPM layers, as shown in Fig. 12b. However, the average thicknesses of the CPM layers after construction were 145 mm for siltstone materials and 130 mm for hornfels, which will be used for the simulation tests. Throughout the experiment, a falling weight deflectometer (FWD) was used to collect pavement deflections at regular stages of loading. It is noted that ALF trafficking occurred over 17 months, during which the typical range of ambient temperatures was expected, spanning from 8 °C in winter to 35 °C in summer. The impact of temperature changes on surface deflection results was already accounted for in the back-calculation analysis of the experimental data [3].

According to Fig. 12b, the sand layer (subgrade layer) located below the cemented base is thicker, making it the main supporting layer for the cemented layer. Additionally, the asphalt layer on top serves as a smooth surface for the ALF load wheels and FWD testing, without significantly affecting the structural capacity of the pavement. Considering these factors, the pavement layers in the ALF test (Fig. 12b) can be simplified into two layers: cemented layer and subgrade layer. The dimensions and applied load positions of the simplified pavement layers are shown in Fig. 13a. The boundary conditions for the ALF test in ABAQUS are illustrated in Fig. 13b. During the simulation, cyclic pressure is applied on a width of 0.1 m, to replicate a load varying from 0 kN to the test load ranging from 40 to 80 kN depending on the numerical tests. The load frequency is set at 3.33 Hz to eliminate inertia effects. To reduce computational costs, only half of the ALF test is simulated using plane-stress 3-node elements (CPS3), with 4410 and 4192 elements for the siltstone and hornfels pavement test, respectively. Besides, the behaviour of the subgrade layer is assumed to be linear elastic in the

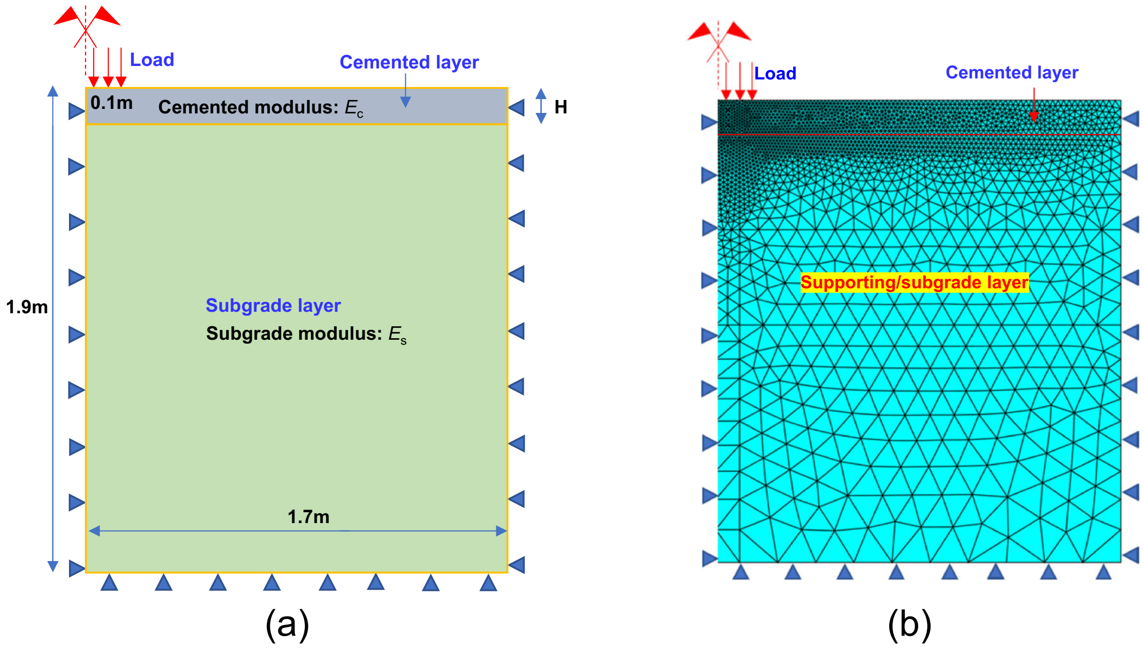

Fig. 13 **a** Simplified pavement layers of ALF test (symmetrical plane stress); **b** Loading and boundary conditions of ALF test in ABAQUS (symmetrical plane stress)

simulation. The elastic properties of the subgrade layer include a modulus (E_s) of 193 MPa and a Poisson's ratio (ν) of 0.4 for simulating siltstone pavement, and E_s = 215 MPa and ν = 0.4 for hornfels pavement. These parameters are calibrated to match the initial deflection of the top surface of the cemented layers obtained from experimental data.

In the 4 PB tests, the initial horizontal tensile strain at the bottom of the beam is calculated using Eq. (24), which is based on beam theory. To ensure consistency with this calculation and ALF experimental data using initial elastic tensile strain at the bottom of the cemented layer, we also use the elastic value obtained from our elastic simulations in calculations, as shown in Fig. 15. Furthermore, it is crucial to determine the reduction in the modulus of the cemented layer. Unlike the 4 PB beam tests, where the beam modulus can be directly calculated using Eq. (26), the modulus of the cemented layer in the ALF tests is determined through a back-calculation method. In the ALF experiments, the moduli of the cemented layers were back-calculated from the FWD data, involving the modelling of the pavement as a linear elastic layered structure [3]. Initially, assumed modulus values and known layer thicknesses were used. The deflection bowl obtained from elastic modelling was compared to the deflection bowl measured by the FWD. An error parameter was calculated based on the differences between these two bowls. The process involved iterative adjustments of the assumed layer moduli to minimise this error by recalculating and comparing the deflection bowls. This back-calculated method was applied to the CPM layers before cracks or ALF loading occurred. Once ALF loading began, the cracked CPM was modelled as a weakened linear elastic layer with a reduced modulus. Therefore, during traffic loading, the equivalent modulus approach (EMP) was utilised. Similarly, EMP was also employed in the simulation tests. However, the deflection of the cemented layer was obtained from our simulation results using the developed fatigue modelling. This deflection is then compared with the deflection obtained from fatigue modelling simulation with a reduced modulus cemented layer. If the difference between these two deflections is similar, the equivalent modulus reduction of the cemented layer is determined.

2.3.2 Simulation results from ALF tests

The evolution of the macro- and meso-scale behaviours of CPMs in the ALF test, under the load level of 40 kN for siltstone materials, is shown in Fig. 14. In the first cycle, zones of horizontal tensile stress and normal traction on the primary cracks develop at the bottom of the cemented layer. As the load cycles increase, these zones expand in size, accompanied by softening behaviour occurring within the cemented layer (Fig. 14a, b). The damage variable, representing the propagation of fatigue cracks, initiates at the bottom of the cemented layer and spreads upwards until the layer fails (Fig. 14c). Similarly, vertical cracks initially appear at the bottom layer and progressively concentrate at the centre of the cemented layer with an increasing number of cycles (Fig. 14d). These findings demonstrate a clear

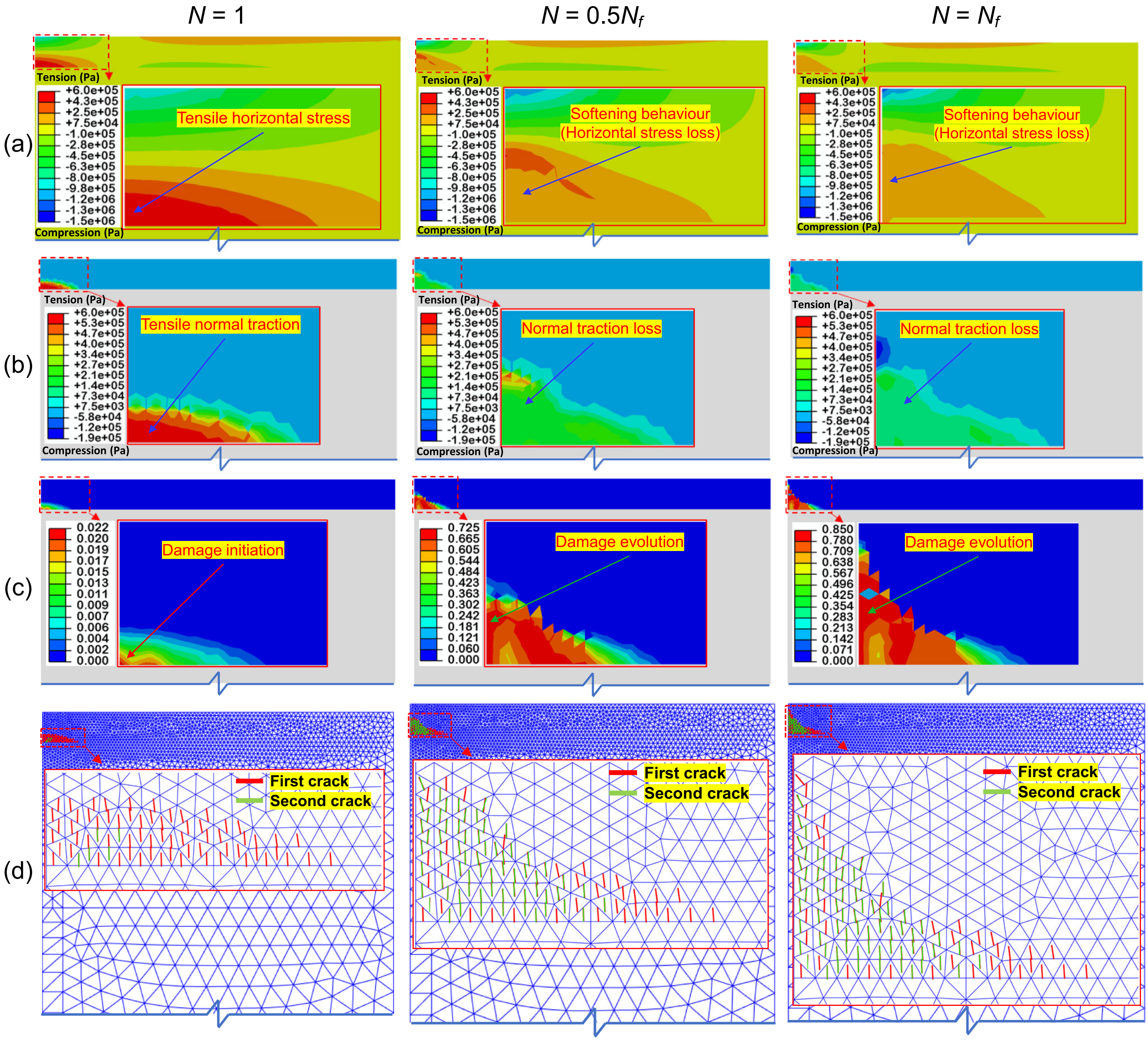

Fig. 14 Details of the ALF test at a load level of 40 kN for siltstone materials under the different number of cycles: **a** Horizontal stress (Pa); **b** Normal traction on primary crack (Pa); **c** Maximum total damage contour profiles; **d** Fatigue crack evolution

bottom-up failure mechanism attributed to fatigue crack growth in the cemented layer at the field scale. Notably, these results align with the experimental findings reported in Austroads [3].

Next, we conducted the ALF tests on two materials at various load levels ranging from 40 to 80 kN. The modulus reduction curves obtained from simulations are presented in Fig. 15a and b, with the corresponding experimental results included for comparison in Fig. 15c and d. The results exhibit three distinct phases observed in both the simulations and experiments. Initially, there is a rapid reduction in modulus, followed by a stable stage, and ultimately reaching a plateau known as the equivalent granular phase [5, 34]. Notably, the third phase observed in the ALF results differs from the one observed in the 4 PB tests (presented in Sect. 2.2.3), where the modulus experienced a quick reduction until the beams ultimately failed under cyclic loads. This disparity can be attributed to the differences in boundary conditions between the laboratory and ALF tests. While the 4 PB tests are supported by two rollers at the bottom of the specimen, the ALF tests are fully supported by the subgrade layer. Consequently, even though the cemented layer predominantly loses its material strength, it does not experience sudden failure as observed in the laboratory tests.

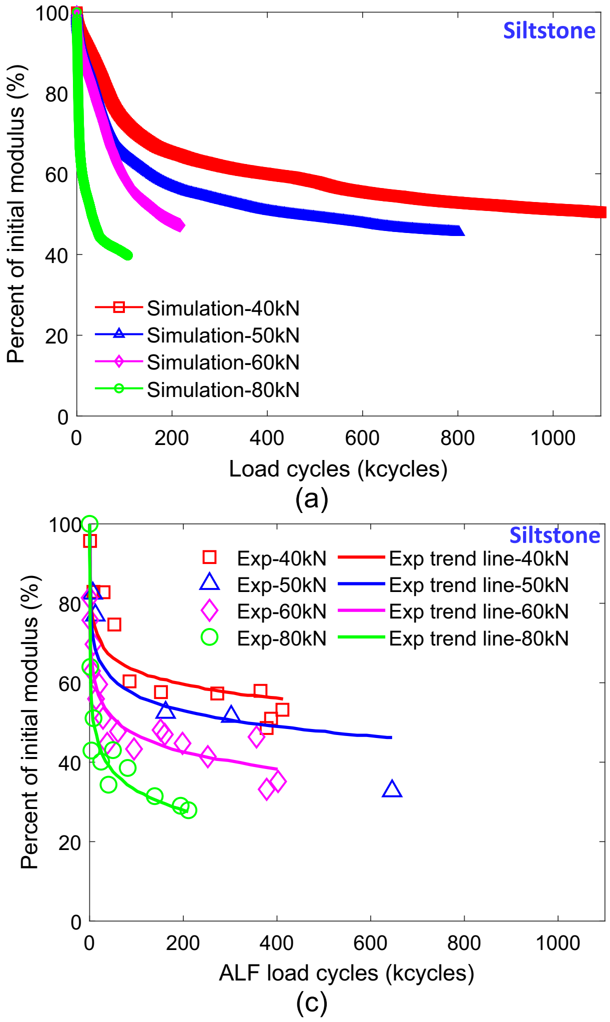

Fig. 15 Comparison between ALF simulation and experimental data in terms of modulus reduction versus the number of ALF cycles: **a** Simulation results for siltstone; **b** Simulation results for hornfels; **c** Experimental data for siltstone; **d** Experimental data for hornfels

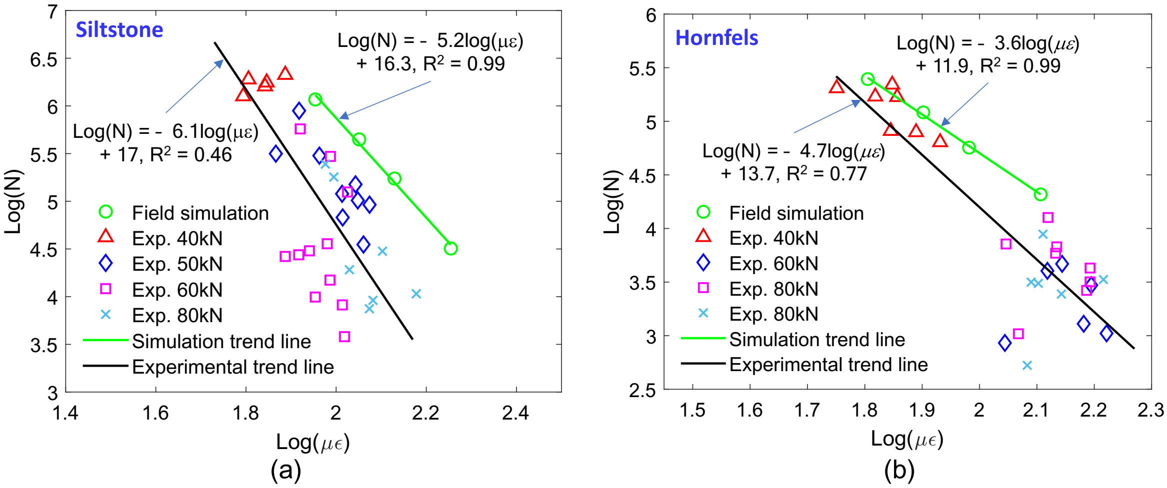

Fig. 16 Comparison of initial micro-tensile strain versus fatigue lives (S-N_f curves) between field-scale simulation and ALF experiments for: **a** Siltstone materials; **b** Hornfels materials

From a qualitative perspective, the simulation results effectively capture the load effects on the fatigue lives of the cemented layer compared to experimental data. Specifically, with increasing applied loads, the simulation modulus reduces rapidly (Fig. 15a and b), which is consistent with the observed trend in the experimental outcomes shown in Fig. 15c and d. Additionally, as the load level increases, the cemented layer exhibits earlier failure (i.e. reaching a 50% reduction in modulus). To assess the quantitative performance of the proposed model, S-N_f curves obtained from simulation results and experimental data are plotted in Fig. 16. The comparison reveals a similar trend between the simulation results and experimental data. The simulation fatigue lives fall within the range of the experimental ones. However, the simulation trend line tends to slightly overestimate the initial strain when compared to the corresponding experimental values. This discrepancy can be attributed to the back-calculation method used to determine the initial tensile strain. While the experimental results are based on an elastic pavement structure using axisymmetric conditions, our method is to derive the initial elastic tensile strain using plane stress conditions. Furthermore, the difference in initial modulus and measured thickness of structural pavement layers used in elastic modelling by ARRB compared to the calibrated modulus of the subgrade layer in our simulation can further contribute to the disparity in initial tensile strain. It is important to note that our aim is not to intentionally fit the simulation results to the experimental data from the ALF tests. Instead, we utilise the same parameters calibrated at the laboratory scale and apply them to the field scale to predict the fatigue performance of CPMs, both under plane stress conditions.

2.4 Development of fatigue shift factors

2.4.1 Mechanism-based lab-to-field fatigue shift factors (M-SFs)

The ultimate objective of this study is to establish a connection between fatigue performance at the laboratory and the field scale using SFs. To achieve this, the S-N_f curves obtained from simulation results of both the laboratory scale (4 PB tests) and the field scale (ALF tests) are plotted in Fig. 17a, c using a logarithmic scale. As observed, there is a shift in the $\log(N_f)$-$\log(\mu\varepsilon)$ relation when transitioning from the laboratory to the field scale. This shift primarily arises from the disparity in boundary conditions between the two scales, which results in distinct failure mechanisms, as explained in Sect. 2.3.2.

According to Austroads [7] and Austroads [9], a strain-based fatigue equation has demonstrated its effectiveness in capturing laboratory and accelerated loading data. Consequently, it has been an integral component of Austroads' design procedures for approximately three decades. This equation can be derived from fatigue results as follows:

$$N = \left(\frac{k}{\mu\varepsilon}\right)^{12} \tag{27}$$

where N is the allowable number of load repetitions from fatigue testing, $\mu\varepsilon$ is the load-induced tensile strain at the base of the test beam or cemented layer (microstrain), and k is a fatigue constant.

The strain damage exponent (SDE) of 12 in Eq. (27) represents an average value obtained from an extensive dataset of fatigue laboratory tests for various CMPs. Accordingly, this value is used in this study. By employing this, the M-SFs for siltstone and hornfels materials are obtained as 1.19 and 1.21, respectively, as illustrated in Fig. 17b and d. Compared to siltstone materials, hornfels materials demonstrate a better fit between laboratory and field results. This discrepancy is attributed to the difference in layer thicknesses; the hornfels layer is 130 mm thick, whereas the siltstone layer is 145 mm thick. As anticipated, smaller horizontal strains were observed in the field for siltstone materials, resulting in variable strain results between the laboratory and the field. It is noted that the obtained SF values result from a rigorous fatigue modelling approach, which undergoes comprehensive validation in the laboratory and demonstrates fair predictions of fatigue performance at the field scale. Furthermore, the consistency in fatigue failure criteria between laboratory and field conditions renders these derived SFs reliable and distinguishes them from previous SFs for CPMs. It is noteworthy that the SFs in this study are derived within the strain-fatigue life space to account for the disparity in strain between laboratory and field scales. The developed M-SF values are smaller in comparison to the strain-based SF of 1.9 as outlined in Austroads [7]. However, this SF relies heavily on experimental data, specifically derived from Mulgrave accelerated loading tests, to account for a threefold reduction in modulus, as detailed in Sects. 3.1 and 7.4 of Austroads [7]. This original value of 1.9 was then adjusted to a recommended SF of 1.8, with a new definition of in-service fatigue life, defined as 1/5th the initial modulus instead of ½ [7]. In other words, this SF is applied to convert laboratory test results, obtained from well-cured beams characterised by low micro-cracking and high modulus, into design models using a design modulus of 1/3rd of the 90-day laboratory measured value. In contrast, M-SF values presented in this section aim to represent the intrinsic shift in fatigue performance from lab-to-field scale. It should be noted that M-SFs are derived from simulation results calibrated with the measured laboratory

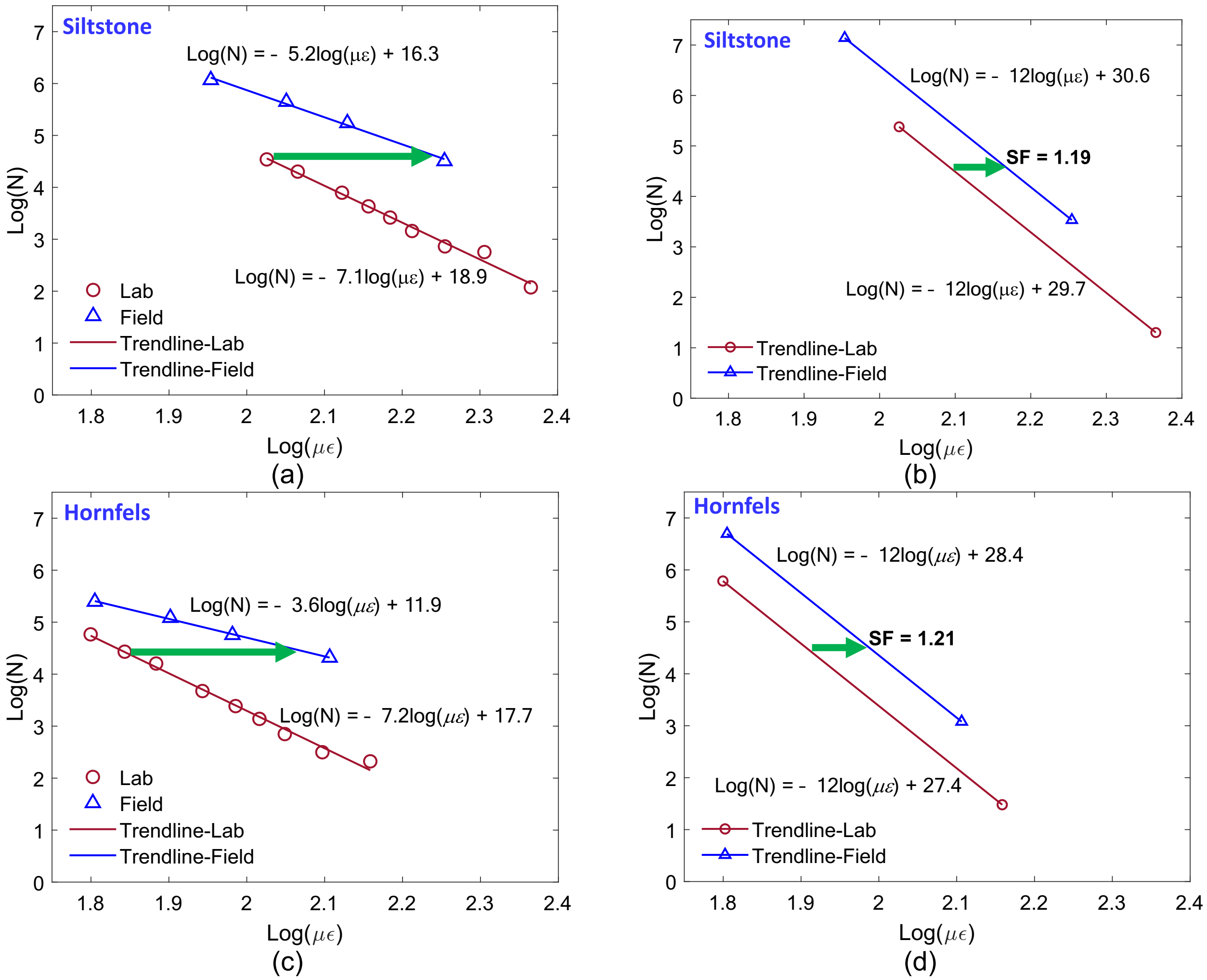

Fig. 17 Shifting in strain and fatigue lives from lab-to-field scale: **a** Lab-to-field shifting for siltstone; **b** Lab-to-field SF for siltstone using SDE of 12; **c** Lab-to-field shifting for hornfels; **d** Lab-to-field SF for hornfels using SDE of 12

fatigue relationships presented in Austroads [2]. These laboratory results were significantly influenced by micro-cracking resulting from disruptions in the moist curing process. Consequently, the M-SF values of 1.19 and 1.21 for siltstone and hornfels, respectively, should be interpreted as applicable to weakened areas in the field that may have experienced micro-cracking prior to loading.

2.4.2 Shift factors due to modulus change of cemented layer

The SFs discussed in Sect. 2.4.1 illustrate the transition of fatigue performance from the laboratory to the field scale. However, in in situ scenarios, the properties of cemented layers can vary from laboratory-measured values due to factors like construction quality, curing conditions or curing time. Thus, this section aims to investigate the impact of modulus changes in the cemented layers on their fatigue lives. To this end, the simulation set-up and model parameters are kept the same for both materials, except for the moduli. Specifically, for siltstone materials, the modulus of the cemented layer varies from 12 to 6 MPa, while for hornfels materials, it ranges from 18 to 6 MPa. Figure 18 illustrates the effect of modulus changes on the log(N_f)-log($\mu\varepsilon$) relationships with the fatigue life N_f reaching a 60% decrease in modulus. This number is chosen since for both siltstone and hornfels material layers with low modulus (i.e. 6MPa), the simulation results cannot reach a 50% decrease in modulus according to Austroads [8]. As can be seen in Fig. 18, there is a shift in the strain versus life relationship from cemented layers with a high modulus to those with a low modulus. This shift occurs because the initial tensile strain at the bottom of the cemented layers increases as the modulus decreases. Referring to Austroads [9] and considering SDE of 12, the SF associated with modulus changes in cemented layers at

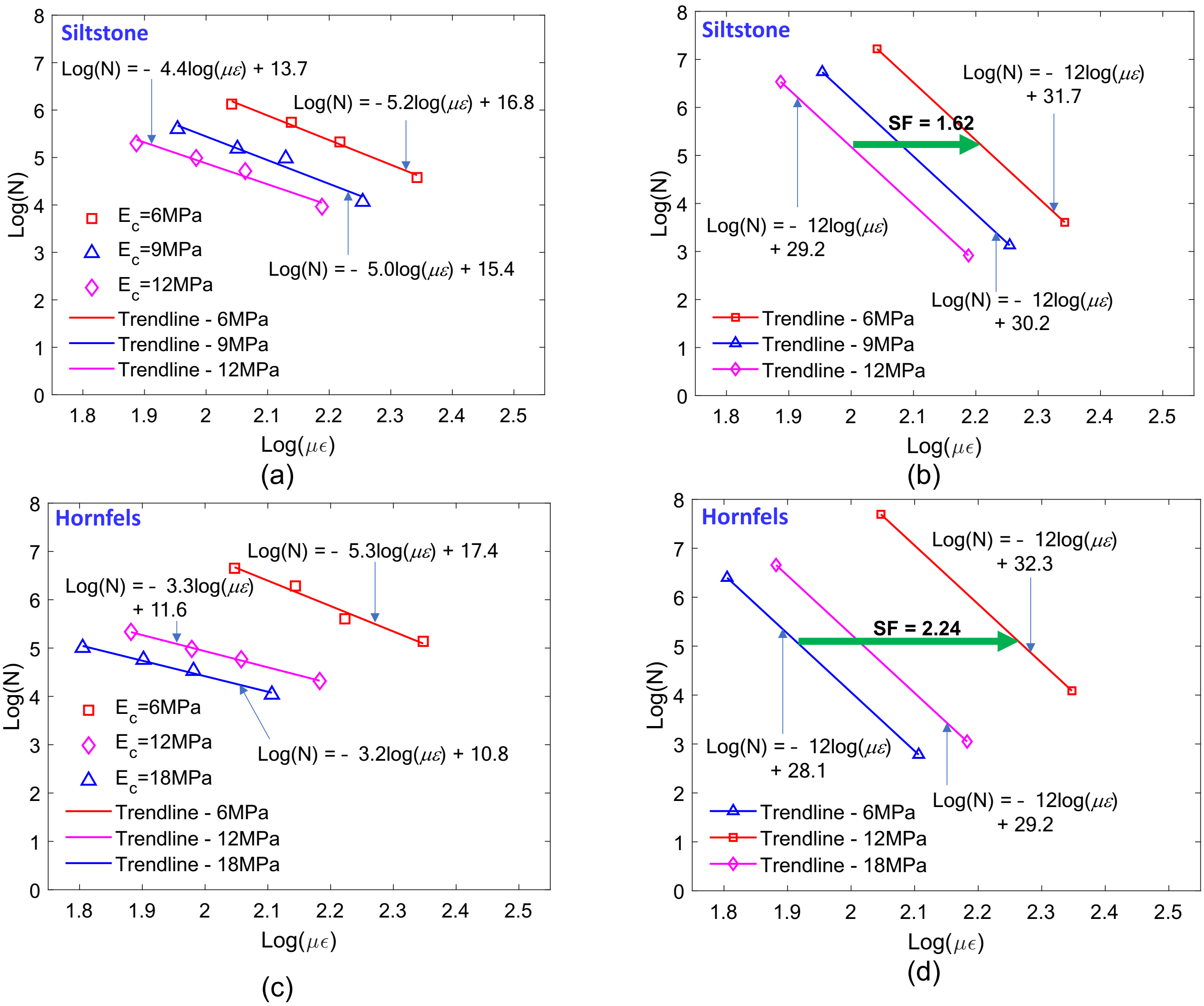

Fig. 18 Effect of cemented layer modulus change on the relationship between initial tensile strain and fatigue life obtained from simulation results **a** Relation for siltstone; **b** Relation for siltstone using SDE of 12; **c** Relation for hornfels; **d** Relation for hornfels using SDE of 12

the field scale for siltstone materials is determined to be 1.62 when the modulus is reduced by a factor of two. Similarly, an SF of 2.24 is identified for hornfels materials when the modulus declines by a factor of three. Additionally, SDE values for both materials tend to increase when the moduli of the cemented layer decrease. Specifically, SDE increases slightly from 4.4 to 5.2 for siltstone material with reducing moduli from 12 to 6 MPa. Similarly, SDE increases significantly from 3.2 to 5.3 for hornfels material with reducing moduli from 18 to 6 MPa.

3 Conclusion

This study proposes a mechanism-based methodology for developing SFs for CPMs. The proposed approach utilises a rigorous two-scale fatigue model to predict and analyse the fatigue performance of CPMs using both 4 PB and ALF tests. Based on a consistent lab-to-field fatigue failure criterion (i.e. modulus reduction of CPMs), strain-based lab-to-field shift factors of 1.19 for siltstone and 1.21 for hornfels materials are determined to account for the difference in strain between lab and field conditions. Additionally, to accommodate modulus reduction in the field, likely caused by construction issues, curing conditions, or curing time, SFs of 1.62 and 2.24, corresponding to two and three times the modulus reduction of the cemented layer, are derived for siltstone and hornfels materials, respectively. Future research should focus on developing more generalised SFs. This should include investigating the effects of moving loads and traffic wander on the fatigue performance of CPMs. Laboratory fatigue tests typically apply loading to the same location on the specimen, while vehicle positions in the field are not constrained.

Furthermore, considering the differences in stress/strain states is essential since laboratory tests typically involve uniaxial or biaxial stress/strain states, whereas triaxial stress/strain states exist in the field. Ultimately, the question of how to combine individual SFs, considering each contributing factor, to formulate an overall SF remains open for further exploration.

Acknowledgements This research work is part of a research project (Project No IH18.02.4) sponsored by the SPARC Hub (https://sparchub.org.au) at the Department of Civil Engineering, Monash University, funded by the Australian Research Council (ARC) Industrial Transformation Research Hub (ITRH) Scheme (Project ID: IH180100010). The financial support from Monash International Scholarship (Le), and the Australian Research Council via Future Fellow Project FT200100884 (Bui) are also gratefully acknowledged. Part of this research was undertaken with the assistance of resources and services from the National Computational Infrastructure (NCMAS-2023-101). Last but not least, we would like to express gratitude to Dr Geoff Jameson (ARRB/NTRO) for his valuable comments on this paper and to Dr Richard Yeo (ARRB/NTRO) for generously providing the experimental data obtained from the Austroads projects.

Author contribution Vinh T. Le: Methodology, Software, Formal Analysis, Investigation, Writing—Original Draft, Visualisation. Ha H. Bui: Conceptualisation, Methodology, Supervision, Software, Investigation, Writing—Review & Editing Funding acquisition, Project administration. Giang D. Nguyen: Conceptualisation, Methodology, Investigation, Writing—Review & Editing. Jayantha Kodikara: Investigation, Writing—Review & Editing, Funding acquisition. Didier Bodin: Investigation, Writing—Review & Editing. James Grenfell: Investigation, Writing—Review & Editing.

Funding Open Access funding enabled and organized by CAUL and its Member Institutions. Australian Research Council, IH180100010, FT200100884, National Computational Infrastructure, NCMAS-2023-101

Data availability No datasets were generated or analysed during the current study.

Declarations

Competing Interests The authors declare no competing interests.

References

1. Al-Qadi IL, Nassar WN (2003) Fatigue shift factors to predict HMA performance. Int J Pavement Eng 4(2):69–76
2. Austroads (2008a) The development and evaluation of protocols for the laboratory characterisation of cemented materials. AP-T101/08, Austroads, Sydney, NSW
3. Austroads (2008b) Fatigue performance of cemented materials under accelerated loading - influence of vertical loading on the performance of unbound and cemented materials. AP-T102/08, Austroads, Sydney, NSW
4. Austroads (2008c) Construction report for cemented test pavements – influence of vertical loading on the performance of unbound and cemented materials. AP-T103/08, Austroads, Sydney, NSW.
5. Austroads (2010) Cost effective structural treatments for rural highways: cemented materials. AP-T168/10, Austroads, Sydney, NSW
6. Austroads (2013) Review of definition of modified granular materials and bound materials. AP-R434–13, Austroads, Sydney, NSW
7. Austroads (2014a) Framework for the revision of austroads design procedures for pavements containing cemented materials. AP-R463–14, Austroads, Sydney, NSW
8. Austroads (2014b) Cemented materials characterisation: final report. AP-R462–14, Austroads, Sydney, NSW
9. Austroads (2017) Guide to pavement technology-part 2: pavement structural design. AGPT02–17, Austroads, Sydney, NSW
10. Austroads (2020) Development of design procedures for lightly bound cemented materials in flexible pavements. AP-R640–20, Austroads, Sydney, NSW
11. Bui HH, Saleh M (2021) Effects of specimen size and loading conditions on the fracture behaviour of asphalt concretes in the SCB test. Eng Fract Mech 242:107452
12. Hill R (1963) Elastic properties of reinforced solids: some theoretical principles. J Mech Phys Solids 11(5):357–372
13. Huang YH (2004) Pavement analysis and design (Vol. 2). Pearson Prentice Hall Upper Saddle River, NJ.
14. Jitsangiam P, Nusit K, Likitlersuang S, Kodikara J (2021) Using damage evaluation to assess the fatigue behaviour of cement-treated base material from laboratory and full-scale performance tests. Transp Geotech 26:100440
15. Le VT, Bui HH, Nguyen GD, Kodikara J, Bodin D, Grenfell J (2023) Meso to macro connections to capture fatigue damage in cemented materials. Int J Fatigue 176:107890
16. Liang J, Ren X, Li J (2016) A competitive mechanism driven damage-plasticity model for fatigue behavior of concrete. Int J Damage Mech 25(3):377–399
17. Liu C, Lv S, Peng X, Zheng J (2019) Normalized characterization method for fatigue behavior of cement-treated aggregates based on the yield criterion. Constr Build Mater 228:117099
18. Lv S, Xia C, Liu H, You L, Qu F, Zhong W, Yang Y, Washko S (2021) Strength and fatigue performance for cement-treated aggregate base materials. Int J Pavement Eng 22(6):690–699
19. Ma Z, Liu L, Yuan Y, Sun L (2019) Estimation of total fatigue life for in-service asphalt mixture based on accelerated pavement testing and four-point bending beam fatigue tests. Can J Civ Eng 46(7):557–566
20. Mandal T, Edil TB, Tinjum JM (2018) Study on flexural strength, modulus, and fatigue cracking of cementitiously stabilised materials. Road Mater Pavement Des 19(7):1546–1562
21. Mateos A, Ayuso JP, Jáuregui BC (2011) Shift factors for asphalt fatigue from full-scale testing. Transp Res Rec 2225(1):128–136

22. Nguyen GD, Bui HH (2020) A thermodynamics-and mechanism-based framework for constitutive models with evolving thickness of localisation band. Int J Solids Struct 187:100–120
23. Nguyen GD, Einav I, Korsunsky AM (2012) How to connect two scales of behaviour in constitutive modelling of geomaterials. Géotech Lett 2(3):129–134
24. Nguyen GD, Korsunsky AM, Einav I (2014) A constitutive modelling framework featuring two scales of behaviour: fundamentals and applications to quasi-brittle failure. Eng Fract Mech 115:221–240
25. Nguyen GD, Nguyen CT, Nguyen VP, Bui HH, Shen L (2016) A size-dependent constitutive modelling framework for localised failure analysis. Comput Mech 58(2):257–280
26. Nusit K, Jitsangiam P, Kodikara J, Bui HH, Leung GLM (2017) Advanced characteristics of cement-treated materials with respect to strength performance and damage evolution. J Mater Civ Eng 29(4):04016255
27. Pai RR, Patel S, Shahu J (2022) Fatigue response of industrial waste mixes for use as cemented base materials in flexible pavement. Int J Geosynth Ground Eng 8(5):61
28. Prowell BD (2010) Estimate of fatigue shift factors between laboratory tests and field performance. Transp Res Rec 2181(1):117–124
29. Ren X, Wei X, Ballarini R (2022) A temporal multiscale model for fatigue damage of concrete. J Eng Mech 148(3):04021163
30. Said SF (1997) Variability in roadbase layer properties conducting indirect tensile test. Statens väg-och transportforskningsinstitut., VTI särtryck 278
31. SANRAL (2013) South African pavement engineering manual-Chapter 10: pavement design. The South African National Road Agency SOC LTD South Africa
32. Sounthararajah A, Bui HH, Nguyen N, Jitsangiam P, Kodikara J (2018) Early-age fatigue damage assessment of cement-treated bases under repetitive heavy traffic loading. J Mater Civ Eng 30(6):04018079
33. Sulem J, Vardoulakis I (1995) Bifurcation analysis in geomechanics. CRC Press
34. Theyse H, De Beer M, Rust F (1996) Overview of South African mechanistic pavement design method. Transp Res Rec 1539(1):6–17
35. Thom N (2008) Principles of pavement engineering. Thomas Telford London, UK
36. Vardoulakis I, Goldscheider M, Gudehus G (1978) Formation of shear bands in sand bodies as a bifurcation problem. Int J Numer Anal Meth Geomech 2(2):99–128
37. Yeo YS (2011) Characterisation of cement-treated crushed rock basecourse for Western Australian roads Curtin University
38. Zhang H, Chen Z, Zhu C, Wei C (2020) An innovative and smart road construction material: Thermochromic asphalt binder. New materials in civil engineering. Elsevier, Amsterdam, pp 691–716. https://doi.org/10.1016/B978-0-12-818961-0.00022-3
39. Zhang J, Bai J, Wang S (2022) Fatigue damage evolution rule of cement stabilized macadam used in pavement's base course at different curing time. Constr Build Mater 325:126827